The University Of Sheffield.

This is a repository copy of *Tubular modular permanent-magnet machines equipped with quasi-Halbach magnetized magnets - Part II: Armature reaction and design optimization* .

White Rose Research Online URL for this paper:
http://eprints.whiterose.ac.uk/822/

**Article:**

Wang, J.B. and Howe, D. (2005) Tubular modular permanent-magnet machines equipped with quasi-Halbach magnetized magnets - Part II: Armature reaction and design optimization. IEEE Transactions on Magnetics, 41 (9). pp. 2479-2489. ISSN 0018-9464

https://doi.org/10.1109/TMAG.2005.854327

**Reuse**

Unless indicated otherwise, fulltext items are protected by copyright with all rights reserved. The copyright exception in section 29 of the Copyright, Designs and Patents Act 1988 allows the making of a single copy solely for the purpose of non-commercial research or private study within the limits of fair dealing. The publisher or other rights-holder may allow further reproduction and re-use of this version - refer to the White Rose Research Online record for this item. Where records identify the publisher as the copyright holder, users can verify any specific terms of use on the publisher's website.

**Takedown**

If you consider content in White Rose Research Online to be in breach of UK law, please notify us by emailing eprints@whiterose.ac.uk including the URL of the record and the reason for the withdrawal request.

White Rose university consortium
Universities of Leeds, Sheffield & York

eprints@whiterose.ac.uk
https://eprints.whiterose.ac.uk/

# Tubular Modular Permanent-Magnet Machines Equipped With Quasi-Halbach Magnetized Magnets—Part II: Armature Reaction and Design Optimization

Jiabin Wang, *Senior Member, IEEE,* and David Howe

Department of Electronic and Electrical Engineering, the University of Sheffield, Sheffield, S1 3JD, U.K.

**Using the analytical formulas derived in Part I for predicting the magnetic field distribution, thrust force, and electromotive force of a three-phase tubular modular permanent-magnet machine equipped with quasi-Halbach magnetized magnets, this paper analyzes the armature reaction field, and addresses issues that are pertinent to the design optimization of the machine. It shows that optimal values of the ratio of the axial length of the radially magnetized magnets to the pole pitch exist for both maximum force capability and minimum force ripple. The utility and accuracy of the analytical predictions and design optimization technique are demonstrated on a 9-slot/10-pole machine.**

***Index Terms*—Design optimization, linear machines, permanent-magnet machines.**

## I. INTRODUCTION

IN Part I of this paper, analytical expressions for predicting the open-circuit flux density components in the air gap of a three-phase tubular modular permanent-magnet (PM) machine have been derived. By integrating the radial flux density component at the stator bore over a tooth pitch, the fluxes in the stator teeth and yoke can be evaluated, using the techniques described in [1]. Thus, for specified values of no-load flux densities in the teeth and yoke, as design inputs, the dimensions of the teeth and yoke can be determined. To account for the effect of core saturation, a fictitious radial air gap, $\Delta G$, may be introduced between the inner bore of the stator and the outer surface of the magnets, as described in [1]. Subsequently, the no-load iron loss of the machine can be calculated analytically, using the method reported in [2]. To facilitate performance evaluation and design optimization, it is essential to determine the armature reaction field and winding inductance, to facilitate the design of the winding for operation from a given supply voltage.

Analytical expressions for predicting the armature reaction field and the self- and mutual inductances of conventional tubular machines have been reported in [1], [3]. In tubular modular machines, however, the fundamental of the stator magnetomotive force (MMF) has fewer poles than that of the permanent-magnet armature, the force being developed by the interaction between a higher order MMF harmonic with the permanent-magnet field. Although a method for predicting the armature reaction field and the self- and mutual inductances of a 9-slot/10-pole tubular modular PM machine has been described [4], a general methodology, which is applicable to all feasible slot/pole number combinations and winding configurations for tubular modular machines, has yet to be reported.

In this paper, generic formulas for evaluating the armature reaction field and inductances of a three-phase tubular modular PM machine are presented, and issues that are pertinent to the design optimization of a machine equipped with quasi-Halbach magnetized magnets are discussed. Detailed finite-element analysis is undertaken to verify the analytical predictions. It is shown that an optimal ratio of the axial length of the radially magnetized magnets to the pole pitch exists which yields either maximum force capability or minimum force ripple. The utility and accuracy of the analytical predictions and design optimization technique are demonstrated on a 9-slot/10-pole machine.

## II. ARMATURE REACTION FIELD AND INDUCTANCES

### A. Current Distribution in Modular Permanent-Magnet Machines

Although there are various possible stator winding configurations for three-phase tubular modular PM machines based on the feasible slot/pole number combinations given in Table II in Part I of the paper, for a given slot/pole number combination the most appropriate configuration is that which yields the maximum winding factor for the working space-harmonic MMF and results in no dc MMF component. This winding configuration can be determined as follows. Letting $N_s$ and $p$ denote the number of slots and the number of pole pairs, respectively, of a feasible slot/pole number combination, and $N_m$ be the largest common factor of $N_s$ and $p$, the three-phase modular winding may be deployed within $N_m$ repeated modular pitches given by $\tau_{\rm mp} = 2p\tau_p/N_m$, where $\tau_p$ is the pole pitch. Each modular pitch contains $N_s/N_m$ slots in which to accommodate the three-phase winding. If the number of slots per phase within a modular pitch is even, then the coils which belong to one phase can be further disposed in two separate sections displaced by half a modular pitch and having opposite polarity. By way of example, for a 10-pole (5 pole pair), 9-slot modular machine, the largest common factor between $N_s$ and $p$ is 1, and the number of slots per phase is 3. Thus, the three-phase winding is deployed within one modular pitch of 10 $\tau_p$ or 9 $\tau_{\rm cp}$, where $\tau_{\rm cp}$ is the slot pitch,

Digital Object Identifier 10.1109/TMAG.2005.854327

0018-9464/$20.00 © 2005 IEEE

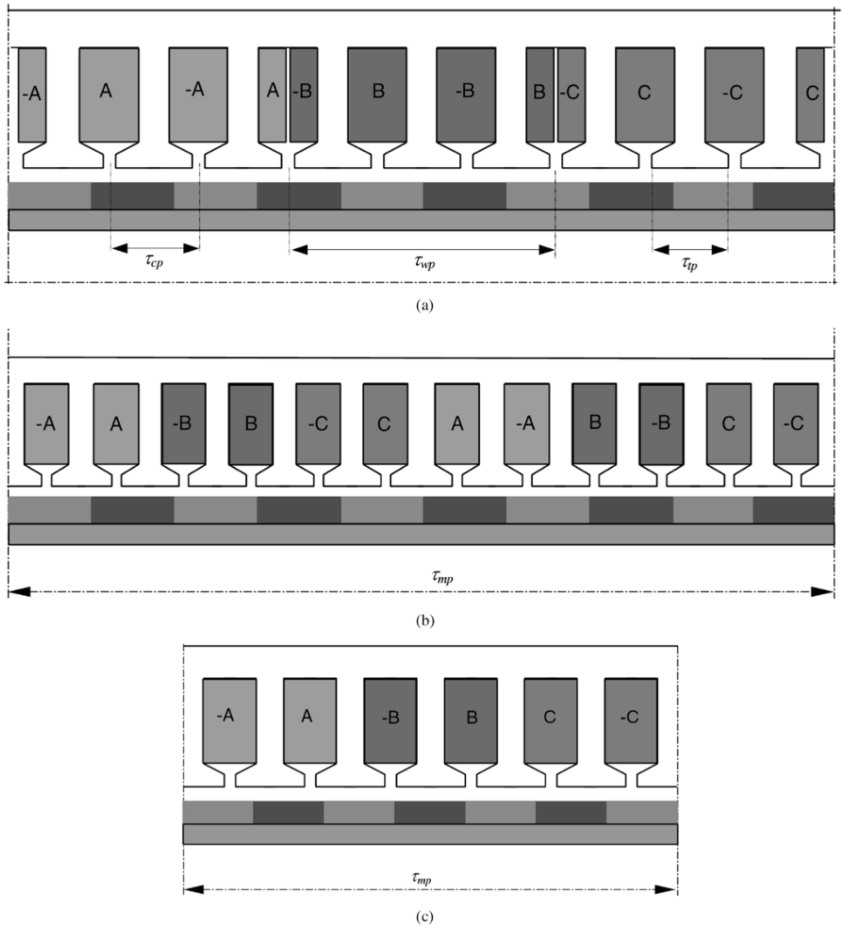


Fig. 1. Winding distributions for three-phase tubular modular PM machines. (a) 10-pole/9-slot machine. (b) 10-pole/12-slot machine. (c) 7-pole/6-slot machine.

which is also equal to the coil pitch, and each phase winding occupies three slots, but has to be accommodated in two full slots and two half slots, as shown in Fig. 1(a), in order to eliminate the dc MMF component. For a 10-pole, 12-slot modular machine, on the other hand, although the largest common factor between $p$ and $N_s$ is also 1, the number of slots per phase is an even number, viz. 4. In order to maximize the winding factor for the working space-harmonic MMF, the phase winding can be subdivided into two sections, each having two slots and displaced from each other by five pole pitches, as shown in Fig. 1(b). For the slot/pole number combinations given in Table III in Part I of the paper, in which the number of active poles, $p_a$, is odd, the winding configuration, can be similarly determined. However, the modular pitch $\tau_{\rm mp}$ is now given by $\tau_{\rm mp} = p_a\tau_p/N_m$, and the coils which belong to one phase have to be arranged adjacent to each other irrespective of whether the number of slots per phase is odd or even. By way of example, Fig. 1(c) shows the winding configuration for a 7-pole, 6-slot modular machine.

Thus, in total there are four possible winding configurations for modular machines over a modular pitch, viz.: (i) in which the number of slots per phase $N_{spm}$ is odd and the coils which belong to one phase are distributed in $(N_{spm} - 1)$ consecutive full slots and in two half slots as is the case in Fig. 1(a); (ii) in which the number of slots per phase is even and the coils which belong to one phase are distributed in two separate winding sections displaced by a half modular pitch and each section has an even number of slots, (i.e., $N_{spm}/2$ is an even number), as is the case in Fig. 1(b); (iii) similar to (i) but in which the number of slots per phase is even, as is the case in Fig. 1(c); and (iv), similar to (ii), but in which each of the two separate winding sections has an odd number of slots.

The current distribution in a slotted stator may be represented by an equivalent current sheet model [5]. Assuming that the yoke and teeth are infinitely permeable, then according to Ampere's law, the Ampere-conductors 2 $N_cI$ in a slot may be represented by an equivalent current sheet 2 $N_cI/b_0$ distributed over the width of the slot opening $b_0$, where 2 $N_c$ is the number of turns of a coil in a full slot. Hence, the MMF distributions which result with the four possible winding configurations for a three-phase tubular modular PM machine are as illustrated in Fig. 2.

It should be noted that in all cases, the reference position of the current sheet distribution is chosen as the center of the phase winding. This allows the current distributions to be expanded into a simple Fourier series of the following form:

$$J_s(z) = \begin{cases} \sum_{n=1}^{\infty} J_n \sin m_{mn} z & \text{Fig. 2(a)–(b)} \\ \sum_{n=1}^{\infty} J_n \cos m_{mn} z & \text{Fig. 2(c)–(d)} \end{cases} \quad (1)$$

where $m_{mn} = 2\,\pi n/\tau_{\mathrm{mp}}$ and $J_n$ can be evaluated by

$$J_n = \begin{cases} \dfrac{2}{\tau_{\mathrm{mp}}}\displaystyle\int_{-\tau_{\mathrm{mp}}/2}^{\tau_{\mathrm{mp}}/2} \mathbf{J}_s(z)\sin m_{mn}z dz & \text{Fig. 2(a)–(b)} \\ \dfrac{2}{\tau_{\mathrm{mp}}}\displaystyle\int_{-\tau_{\mathrm{mp}}/2}^{\tau_{\mathrm{mp}}/2} J_s(z)\cos m_{mn}z dz & \text{Fig. 2(c)–(d)} \end{cases} \quad (2)$$

which yields (3)–(5), shown at the bottom of the page.

### B. Armature Reaction Field

For a tubular modular machine in which the magnets are mounted on a ferromagnetic supporting tube, the armature reaction field and the self- and mutual inductances can be predicted using the techniques and expressions reported in [4] based on the current sheet model established in (1), and (2)–(5). The following derivation is therefore aimed at establishing a framework for predicting the armature reaction field and inductances of the machines in which the magnets are mounted on a nonmagnetic supporting tube.

The effect of slotting can be taken into account by assuming an equivalent stator bore radius $R_{\mathrm{se}}$, as has been shown in [1]. If for simplicity, the relative recoil permeability of the magnets is assumed to be 1, i.e., $\mu_r = 1$, the armature reaction field may be deduced from the model shown in Fig. 3. The governing field equation, in terms of the vector magnetic potential $A_\theta$, is given by

$$\frac{\partial}{\partial z}\left(\frac{1}{r}\frac{\partial}{\partial z}(rA_\theta)\right) + \frac{\partial}{\partial r}\left(\frac{1}{r}\frac{\partial}{\partial r}(rA_\theta)\right) = 0. \quad (6)$$

The boundary conditions to be satisfied by (6) are

$$B_z|_{r=R_{\mathrm{se}}} = \mu_0 \mathbf{J}_s(z); \qquad B_r|_{r=0} = 0. \quad (7)$$

Solving (6) subject to the boundary conditions of (7) yields the following expressions for $A_\theta$ and the flux density components:

$$A_\theta = \begin{cases} \displaystyle\sum_{n=1,2,\ldots} \frac{1}{m_{mn}}\{a_n BI_1(m_{mn}r)\}\sin m_{mn}z & \text{Fig. 2(a)–(b)} \\ \displaystyle\sum_{n=1,2,\ldots} \frac{1}{m_{mn}}\{a_n BI_1(m_{mn}r)\}\cos m_{mn}z & \text{Fig. 2(c)–(d)} \end{cases} \quad (8)$$

$$B_r(r,z) = \begin{cases} -\displaystyle\sum_{n=1,2,\ldots}^{\infty} [a_n BI_1(m_{mn}r)]\cos(m_{mn}z) & \text{Fig. 2(a)–(b)} \\ \displaystyle\sum_{n=1,2,\ldots}^{\infty} [a_n BI_1(m_{mn}r)]\sin(m_{mn}z) & \text{Fig. 2(c)–(d)} \end{cases}$$

$$B_z(r,z) = \begin{cases} \displaystyle\sum_{n=1,2,\ldots}^{\infty} [a_n BI_0(m_{mn}r)]\sin(m_{mn}z) & \text{Fig. 2(a)–(b)} \\ \displaystyle\sum_{n=1,2,\ldots}^{\infty} [a_n BI_0(m_{mn}r)]\cos(m_{mn}z) & \text{Fig. 2(c)–(d)} \end{cases} \quad (9)$$

where $BI_0(\cdot)$ and $BI_1(\cdot)$ are modified *Bessel* functions of the first kind of order 0 and 1, respectively. The harmonic field coefficient $a_n$ is given by

$$a_n = \mu_0 J_n / BI_0(m_{mn}R_{\mathrm{se}}). \quad (10)$$

---

$$J_n = \frac{2N_c I}{\tau_p} K_{dmn} K_{pmn} \quad (3)$$

$$K_{dmn} = \frac{\sin(m_{mn}b_0/2)}{(m_{mn}b_0/2)} \quad (4)$$

$$K_{pmn} = \begin{cases} \dfrac{2\tau_p}{\tau_{\mathrm{mp}}}\left[2\displaystyle\sum_{j=1}^{\frac{N_{spm}-1}{2}} (-1)^{j+1}\sin\left(\frac{N_{spm}}{2} - j\right) m_{mn}\tau_{\mathrm{cp}} + (-1)^{\frac{N_{spm}-1}{2}}\sin\left(\frac{N_{spm}m_{mn}\tau_{\mathrm{cp}}}{2}\right)\right] & \text{Fig. 2(a)} \\ \dfrac{4\tau_p}{\tau_{\mathrm{mp}}}\left[\displaystyle\sum_{j=1}^{\frac{N_{spm}}{2}} (-1)^{j+1}\sin\left(\frac{N_{spm}}{2} - j\right) m_{mn}\tau_{\mathrm{cp}}\right] & \text{Fig.2(b)} \\ \dfrac{4\tau_p}{\tau_{\mathrm{mp}}}\sin\left(\dfrac{m_{mn}\tau_{\mathrm{mp}}}{4}\right)\left[2\displaystyle\sum_{j=1}^{\frac{N_{spm}-2}{4}} (-1)^{j}\sin\left(\frac{N_{spm}}{4} - j\right) m_{mn}\tau_{\mathrm{cp}} + (-1)^{\frac{N_{spm}+2}{2}}\sin\left(\frac{N_{spm}m_{mn}\tau_{\mathrm{cp}}}{4}\right)\right] & \text{Fig. 2(c)} \\ \dfrac{8\tau_p}{\tau_{\mathrm{mp}}}\sin\left(\dfrac{m_{mn}\tau_{\mathrm{mp}}}{4}\right)\left[\displaystyle\sum_{j=1}^{\frac{N_{spm}}{4}} (-1)^{j}\sin\left(\frac{N_{spm}}{4} - j\right) m_{mn}\tau_{\mathrm{cp}}\right] & \text{Fig. 2(d)} \end{cases} \quad (5)$$

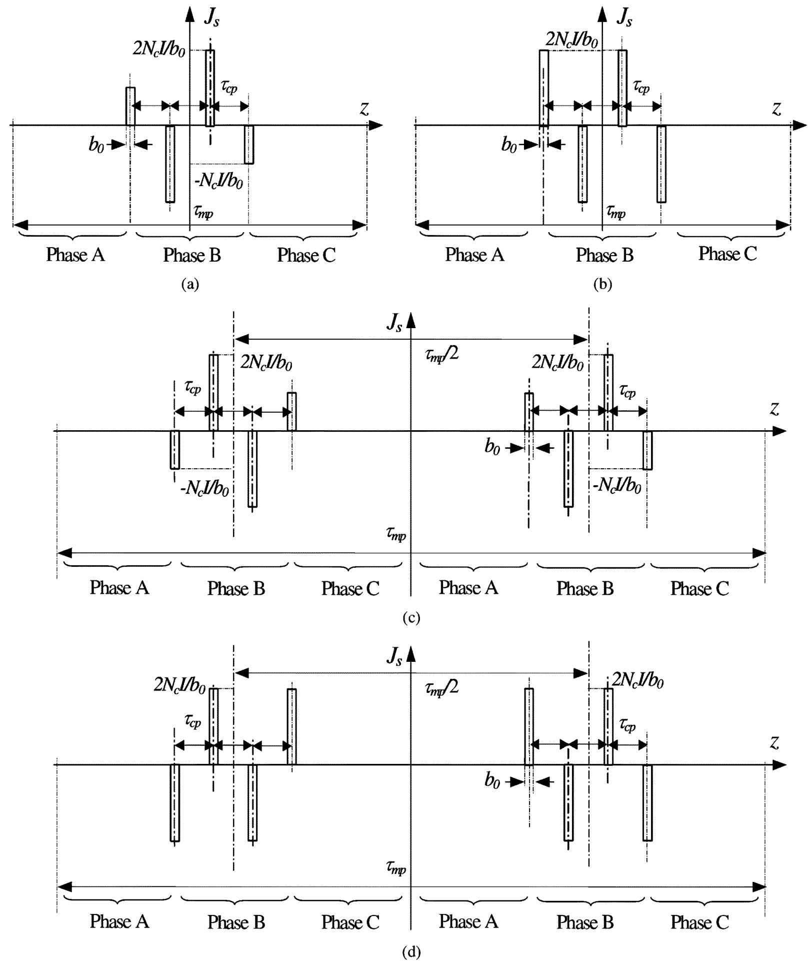


Fig. 2. Equivalent current distributions due to one phase winding over a modular pitch. (a) $N_{spm}$ = odd number. (b) $N_{spm}$ = even number. (c) $N_{spm}/2$ = odd number. (d) $N_{spm}/2$ = even number.

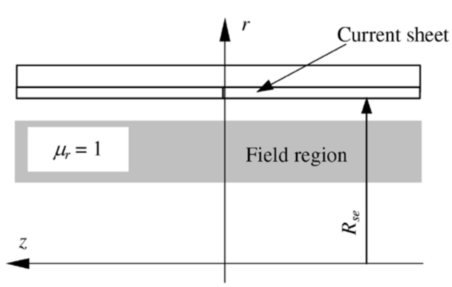


Fig. 3. Armature reaction field model.

## C. Self- and Mutual Inductances

The air-gap self-inductance, $L_{\rm as}$, and the mutual inductance, $M_{aij}$, between phases $i$ and $j(i \neq j)$ separated by an axial displacement $\tau_{ij}$ can be obtained by evaluating the flux-linkage due to the armature reaction field [4], and are given by

$$L_{\rm as} = \frac{8\mu_0 p\pi R_{se} N_c^2}{\tau_p} \times \sum_{n=1,2,\ldots}^{\infty} \frac{(K_{dmn}K_{pmn})^2}{m_{mn}} \left\{\frac{BI_1(m_{mn}R_{se})}{BI_0(m_{mn}R_{se})}\right\} \tag{11}$$

$$M_{aij} = \frac{8\mu_0 p\pi R_{se} N_c^2}{\tau_p} \times \sum_{n=1,2,\ldots}^{\infty} \frac{(K_{dmn}K_{pmn})^2}{m_{mn}} \left\{\frac{BI_1(m_{mn}R_{se})}{BI_0(m_{mn}R_{se})}\right\} \cos m_{mn}\tau_{ij}. \tag{12}$$

For a slotted armature, however, slot-leakage flux will also contribute to the self- and mutual inductances. The self- and mutual slot-leakage inductances, $L_{sk}$ and $M_{sk}$, can be evaluated using the formulas given in [1], and the total self-and mutual inductances are given by

$$\begin{aligned} L_{ps} &= L_{as} + L_{sk} \\ M_{\rm ij} &= M_{aij} + M_{sk}. \end{aligned} \tag{13}$$

It should be noted that the synchronous inductance of the machine is given by $L_{ps} + M_{\rm ij}$, which is an essential parameter in a *d–q* axis model for dynamic simulations and current control loop design, as well as for evaluating the power factor of the machine and the associated converter loss.

## D. Demagnetization Field

The demagnetizing field results from the combined effect of the balanced three-phase winding currents. Further, in order to

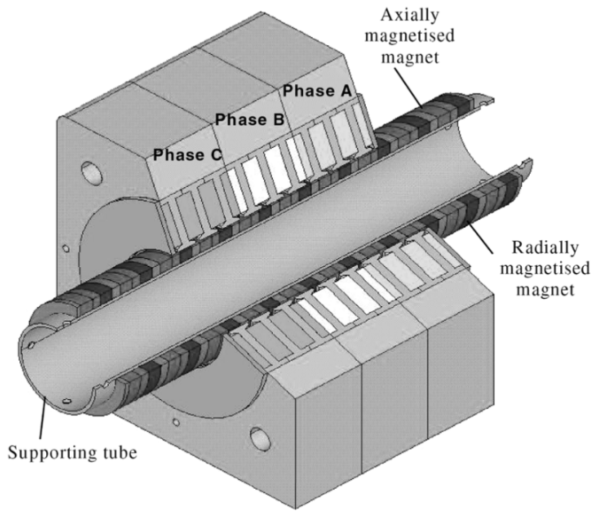


Fig. 4. Schematic of three-phase, 10-pole, 9-slot tubular modular PM machine.

TABLE I
LEADING DESIGN PARAMETERS OF TUBULAR MACHINE

| | | | |
|---|---|---|---|
| $R_{se}$ (m) | 0.0255 | $\tau_{mr}/\tau_p$ | 0.6 |
| $R_m$ (m) | 0.0245 | $b_0$ (m) | 0.002 |
| $h_m$ (m) | 0.005 | $\tau_{cp}$(m) | 0.0111 |
| $G$ (m) | 0.001 | $N_c$ | 30 |
| $\tau_p$ (m) | 0.01 | | |

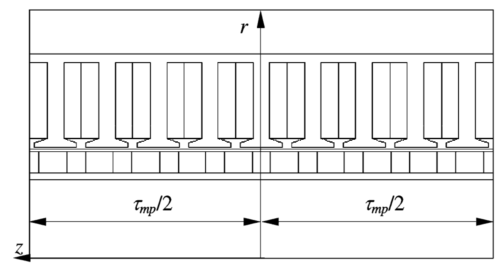


Fig. 5. Finite-element model.

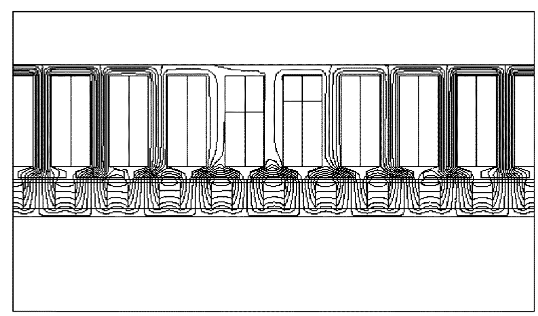
(a)

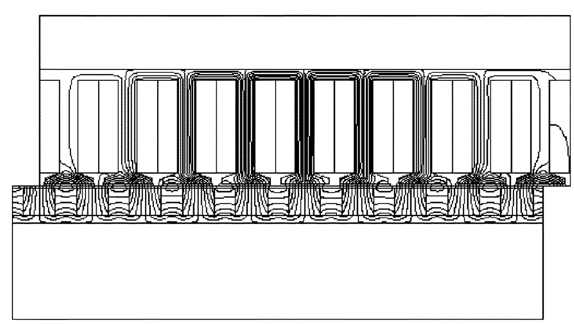
(b)

Fig. 6. Open-circuit flux distributions for two axial displacements. (a) $z_d = 0$. (b) $z_d = \tau_p/2$.

produce a continuous thrust force, the angular frequency of the stator currents must be synchronized with the armature velocity $v$, i.e., $\omega = \pi v/\tau_p$. If the relative velocity between the permanent-magnet armature and the stator is $v$, the axial position $z$ referred to the stationary reference frame may be transformed into the moving reference frame by $z = z_r + vt$. Thus, the flux density components in the moving reference frame for the current distributions shown in Fig. 2(a)–(b) become

$$\begin{aligned} &B_r(r, z_r, t) \\ &= -\frac{3I_m}{2}\left\{\sum_{n=3k+1}^{\infty}[a_n BI_1(m_n r)]\cos\left[m_n z_r + \frac{\pi(n-1)}{\tau_p}vt\right]\right. \\ &\quad \left. - \sum_{n=3k+2}^{\infty}[a_n BI_1(m_n r)]\cos\left[m_n z_r + \frac{\pi(n+1)}{\tau_p}vt\right]\right\} \\ &B_z(r, z_r, t) \\ &= \frac{3I_m}{2}\left\{\sum_{n=3k+1}^{\infty}[a_n BI_0(m_n r)]\cos\left[m_n z_r + \frac{\pi(n-1)}{\tau_p}vt\right]\right. \\ &\quad \left. - \sum_{n=3k+2}^{\infty}[a_n BI_0(m_n r)]\cos\left[m_n z_r + \frac{\pi(n+1)}{\tau_p}vt\right]\right\} \\ &\qquad k = 0, 1, 2, \ldots \end{aligned} \tag{14}$$

where $I_m$ is the peak phase current. Equation (14) can be used to determine the extent, if any, of partial irreversible demagnetization of the magnets under any specified operating condition. A similar expression can be obtained for the current distributions shown in Fig. 2(c)–(d).

## III. Comparison With Finite-Element Analysis

Analytical predictions have been obtained for a 10-pole/9-slot, three-phase tubular modular PM machine with quasi-Halbach magnetized magnets mounted on a mild steel supporting tube (Fig. 4), for which the main design parameters are given in Table I. The stator extends over five active pole pairs, and the magnets are sintered NdFeB with a remanence $B_{\text{rem}} = 1.0486$ T and $\mu_r = 1.05$. Predictions from the derived analytical expressions for the electromotive force (EMF), thrust force, and armature reaction field have been validated by finite-element analysis of the machine using the model shown in Fig. 5.

A periodic boundary condition is applied at the axial boundaries $z = \pm\tau_{\text{mp}}/2$ and the natural Dirichlet boundary condition is imposed at the other boundary surfaces. Saturation of the stator core and the armature supporting tube was accounted for by using the $B$–$H$ curves for the relevant ferromagnetic materials. Thus, the finite-element model takes account of all key effects, such as nonlinearity and slotting, which a practical machine may exhibit.

Fig. 6 shows FE predicted open-circuit flux distributions for two armature displacements, viz. $z_d = 0$ and $z_d = \tau_p/2$, while

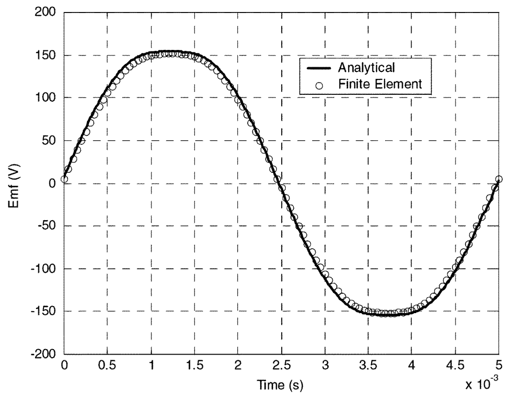


Fig. 7. Comparison of EMF waveforms at $v = 4$ m/s.

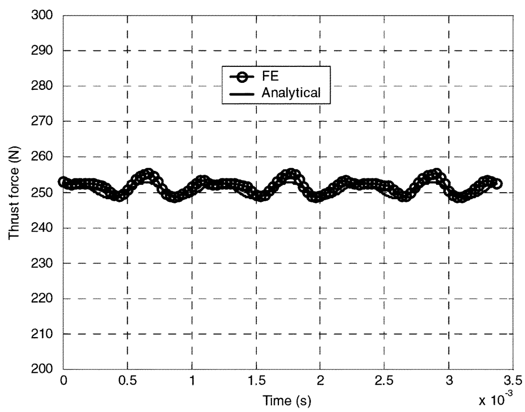


Fig. 8. Variation of thrust force as a function of armature position at rated rms current of 4.35 A.

Fig. 7 compares analytically predicted and finite-element-calculated EMF waveforms for a constant armature velocity of 4 m/s. As will be seen, excellent agreement is achieved. It is also evident from Fig. 6 that the axially magnetized magnets essentially provide a return path for the radial air-gap flux. Hence, the flux in the inner supporting tube is relatively small. The analytically predicted and finite-element-calculated thrust force, at rated current, are compared in Fig. 8. Again, good agreement is achieved in both the amplitude and the waveform. It will be noted that both models predict a very small force ripple. In the analytical prediction, this ripple is due mainly to the presence of fifth and seventh harmonics in the EMF waveform. However, the FE calculation includes two additional effects, viz. a tooth ripple cogging force and localized saturation, which are not accounted for in the analytical model. It follows, however, that since the total peak-to-peak force ripple is less than 2.5%, the tooth ripple cogging force component is extremely low.

Fig. 9 shows the space-harmonic MMF distribution which results from the three-phase stator winding, normalized to the Ampere-turns per slot divided by the width of the slot openings $(N_c I/b_0)$. When the stator winding is excited with balanced three-phase currents, the resultant stator MMF produces forward traveling harmonics of order $n = 1, 4, 7, \ldots$, backward traveling harmonics for $n = 2, 5, 8, \ldots$, and zero triple harmonics. For a 10-pole machine, the thrust force is developed by the interaction of the fifth space harmonic MMF with the field

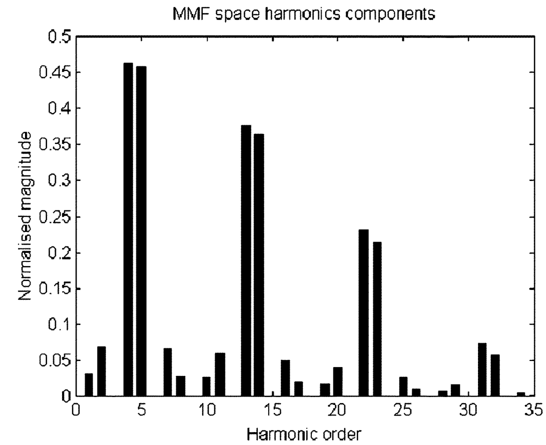


Fig. 9. Normalized space-harmonic MMF distribution for the 10-pole, 9-slot modular machine.

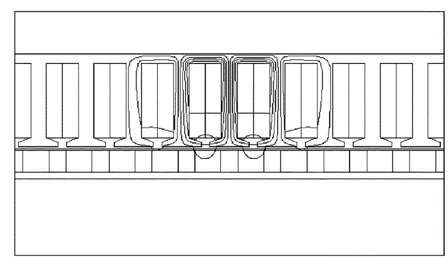

Fig. 10. Flux plot when phase B excited with rated current.

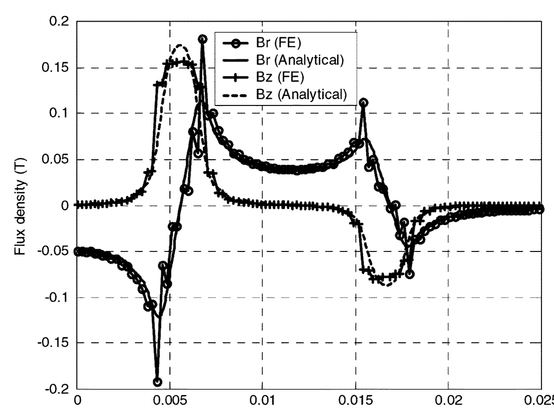


Fig. 11. Variation of air-gap flux density components with axial position at $r = 0.025$ m when phase B excited with rated current.

of the permanent magnets. Fig. 10 shows the armature reaction field distribution when phase $B$ is excited with rated current, while Fig. 11 compares analytically and FE predicted flux density components in the middle of the air gap as functions of axial position. As will be seen, the analytical predictions agree well with results from FE analysis, the main discrepancy being attributable to the neglect of the slot openings in the analytical model.

## IV. Design Optimization

The design of a three-phase tubular modular PM machine can be optimized with respect to the leading design parameters shown in Fig. 12, taking account of both core saturation

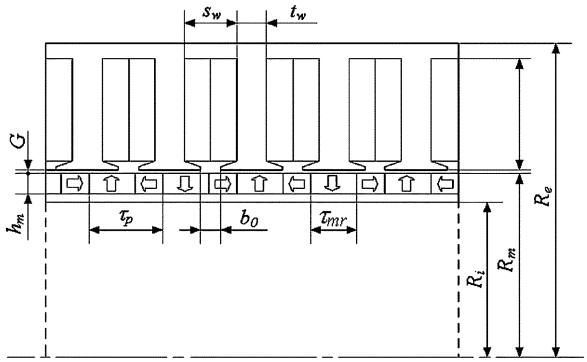


Fig. 12. Leading design parameters of three-phase tubular modular PM machine.

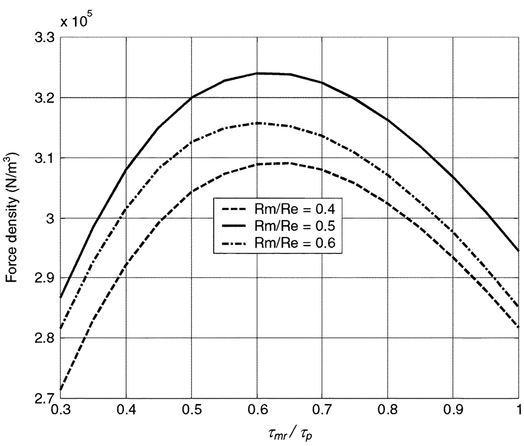


(a)

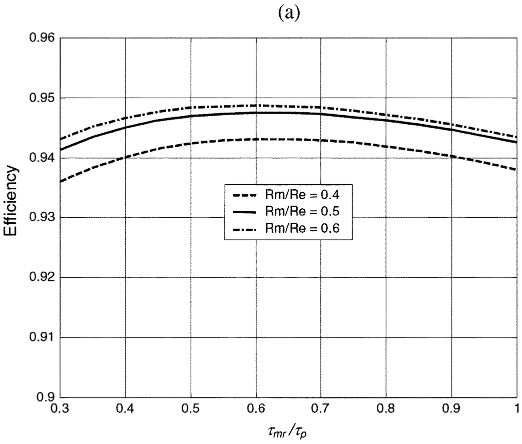


(b)

Fig. 13. Variation of force density and efficiency with $\tau_{\rm mr}/\tau_p$ and $R_m/R_e$. (a) Force density. (b) Efficiency.

TABLE II
FIXED DESIGN PARAMETERS AND OPERATIONAL CONDITIONS

| | |
|---|---|
| Outer stator radius $R_e$ (m) | 0.05 |
| Magnet thickness $h_m$ (m) | 0.005 |
| Air-gap length $G$ (m) | 0.001 |
| Number of pole-pairs $p$ | 5 |
| Number of slots $N_s$ | 9 |
| Magnet remanence $B_{rem}$ (T) | 1.049 |
| Packing factor $P_f$ | 0.5 |
| Ambient temperature ($^0$C) | 40 |
| Temperature rise ($^0$C) | 100 |
| Surface convection coefficient (W/$^0$C/m$^2$) | 20 |
| Rated velocity (m/s) | 6 |

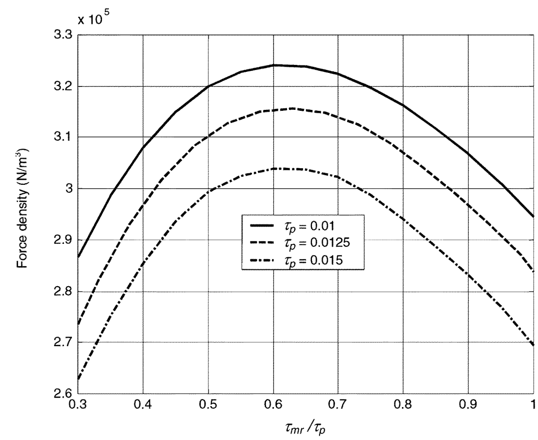


(a)

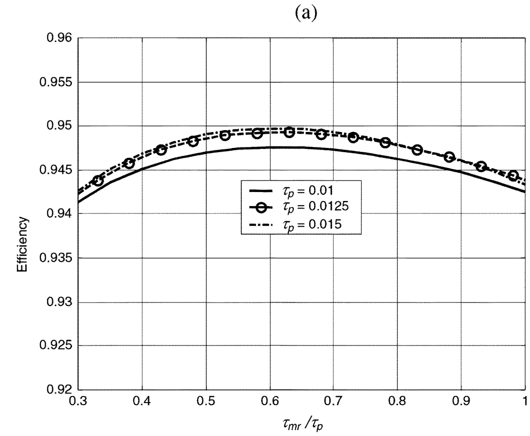


(b)

Fig. 14. Variation of force density and efficiency with $\tau_{\rm mr}/\tau_p$ and $\tau_p$. (a) Force density. (b) Efficiency.

and subject to a specified thermal constraint [1], $R_e$ being the outer radius of the stator and $G$ the air-gap length. It should be noted that the required tooth width $t_w$ and radial thickness of the stator yoke and ferromagnetic supporting tube are dependent on the air-gap flux density and maximum permissible flux density in the yoke and tube. In order that the findings are independent of machine size, the thrust force due to the fundamental component of the radial air-gap field is divided by the volume of the stator, $2\pi p\tau_p R_e^2$, to give the force density (i.e., force per unit volume). In many applications, multiple design objectives are often sought, for example, to maximize the force density or efficiency for minimum cost, and the criteria which are used to judge an optimal machine design may vary from one application to another. In order that the findings are generic, therefore, the following study focuses on the influence of leading design parameters on key cost and performance indicators, such as force/power density, efficiency, normalized force ripple, and power factor, rather than on a specific objective. It is worth noting, however, that when considering design optimization of a complete machine and drive system, the power electronic converter rating and losses should also be taken into account, as they can have a significant influence on the outcome of a design optimization [1].

For a given stator outer radius $R_e$, the design parameters that have the most significant influence on the performance are the

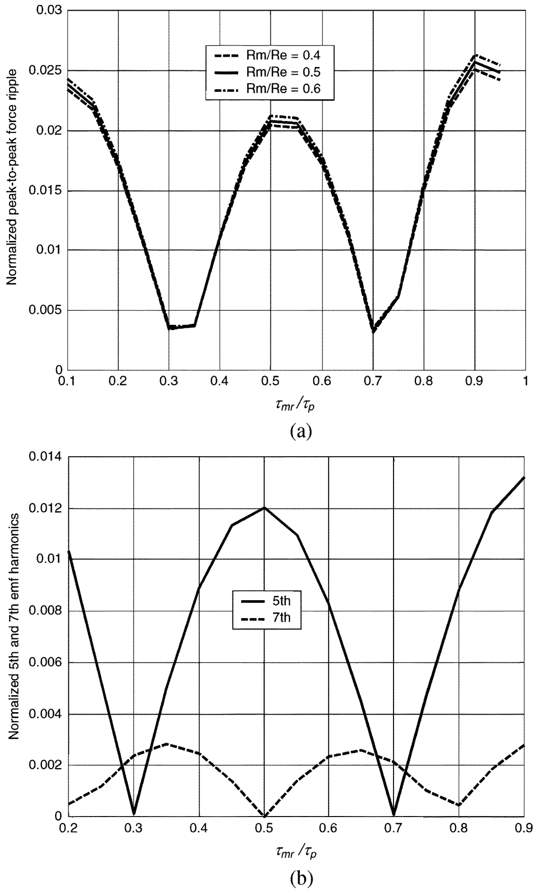


Fig. 15. Variation of normalized peak-to-peak force ripple and fifth and seventh EMF harmonics with $\tau_{\rm mr}/\tau_p$ and $R_m/R_e$. (a) Normalized peak-to-peak force ripple. (b) Fifth and seventh EMF harmonics.

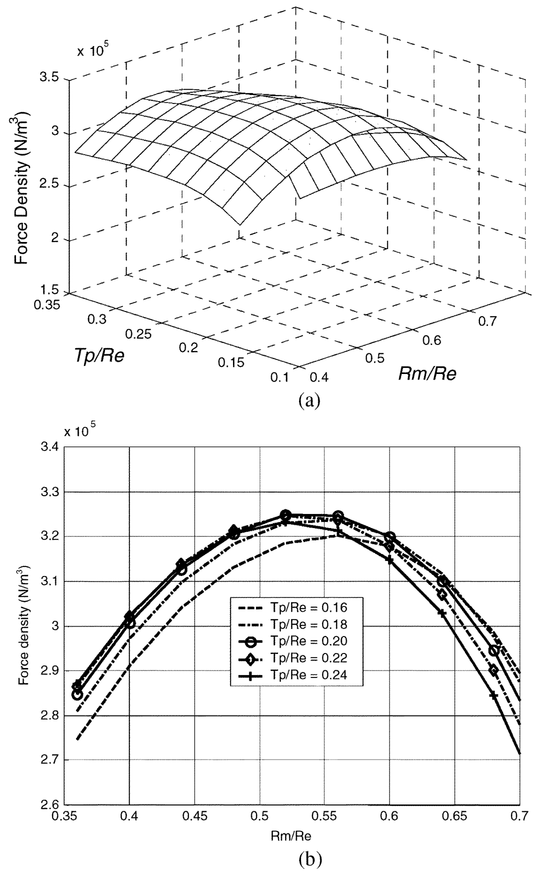


Fig. 16. Variation of force density with $R_m/R_e$ and $\tau_p/R_e$, for $\tau_{\rm mr}/\tau_p = 0.6$. (a) 3-D representation. (b) 2-D representation.

dimensional ratios $R_m/R_e, \tau_p/R_e, \tau_{\rm mr}/\tau_p$, the magnet thickness $h_m$, and the air-gap length $G$. In general, the performance improves as $h_m$ is increased. However, an increase in the volume of permanent-magnet material will increase the cost, particularly if it is a rare-earth magnet, and result in a heavier armature, which is usually undesirable for a moving-magnet machine. In this study, therefore, the magnet thickness is fixed at 5 mm to produce an acceptable air-gap flux density and force density, while providing the required demagnetization withstand capability. The air-gap length $G$ is also assumed to be constant, at 1 mm, since although a smaller air gap would also improve the performance, ultimately it is limited by manufacturing tolerances as well as stiffness and static and dynamic radial run-out considerations.

Fig. 13 shows the variation of the force density and efficiency as functions of $\tau_{\rm mr}/\tau_p$ and $R_m/R_e$, assuming $\tau_p = 0.01$ m. The other fixed design parameters and operational conditions are given in Table II. Similarly, Fig. 14 shows the variation of the force density and efficiency as functions of $\tau_{\rm mr}/\tau_p$ for three different values of $\tau_p$, with $R_m/R_e = 0.5$. As will be seen, in all cases and irrespective of the value of $\tau_p$ and the ratio of $R_m/R_e$, there is an optimal ratio of $\tau_{\rm mr}/\tau_p \approx 0.6$ which yields maximum force density and machine efficiency. This ratio represents an optimal condition under which the combined effect of the radially and axially magnetized magnets results in maximum fundamental radial flux density in the air gap.

Fig. 15(a) shows the variation of the normalized peak-to-peak force ripple as a function of $\tau_{\rm mr}/\tau_p$ and $R_m/R_e$ assuming $\tau_p = 0.01$ m, while Fig. 15(b) shows the variation of the normalized fifth and seventh EMF components with $\tau_{\rm mr}/\tau_p$ when $\tau_p = 0.01$ m and $R_m/R_e = 0.5$. It will be observed again that, irrespective of the ratio of $R_m/R_e$, the normalized peak-to-peak force ripple has two localized minima at $\tau_{\rm mr}/\tau_p \approx 0.3$ and $0.7$. These two minima coincide with the minimum fifth harmonic content in the EMF waveform, as is evident from Fig. 15(b). Indeed, it can be shown, using (8) in Part I of the paper, that the fifth harmonic air-gap flux density component becomes zero when $\tau_{\rm mr}/\tau_p = 0.3$ or $0.7$. Since the magnitude of the fifth EMF harmonic which results with other ratios of $\tau_{\rm mr}/\tau_p$ is much greater than that of the seventh EMF harmonic, the peak-to-peak force ripple is dominated by the influence of the fifth EMF harmonic. The force ripple is therefore a minimum when the fifth harmonic air-gap flux density component is zero. It is also of interest to note that the normalized seventh EMF harmonic has three localized minima, viz. when $\tau_{\rm mr}/\tau_p = 0.2, 0.5$, and $0.8$.

Fig. 16 shows the variation of the force density as a function of $R_m/R_e$ and $\tau_p/R_e$, when $\tau_{\rm mr}/\tau_p = 0.6$. As will be seen, for a given value of $\tau_p/R_e$, there is an optimal $R_m/R_e$ ratio which yields the maximum force density. This ratio represents an optimal balance between the electric loading and the

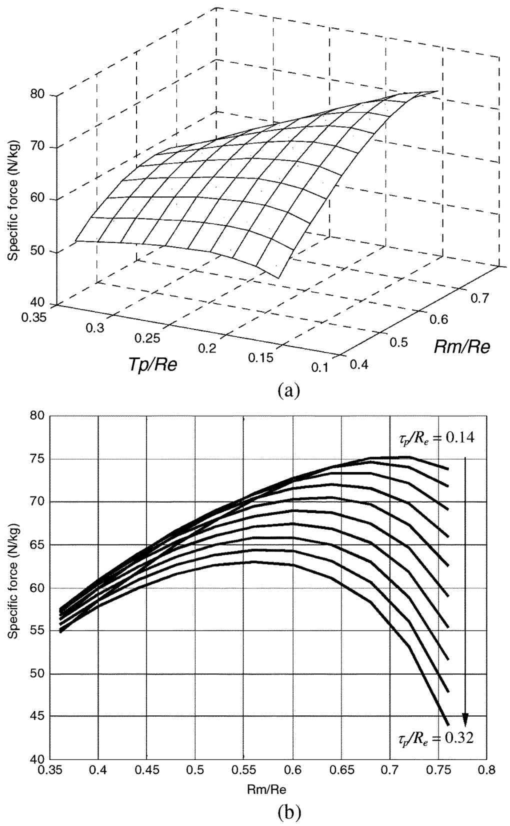


Fig. 17. Variation of specific force with $R_m/R_e$ and $\tau_p/R_e$, for $\tau_{\rm mr}/\tau_p = 0.6$. (a) 3-D representation. (b) 2-D representation.

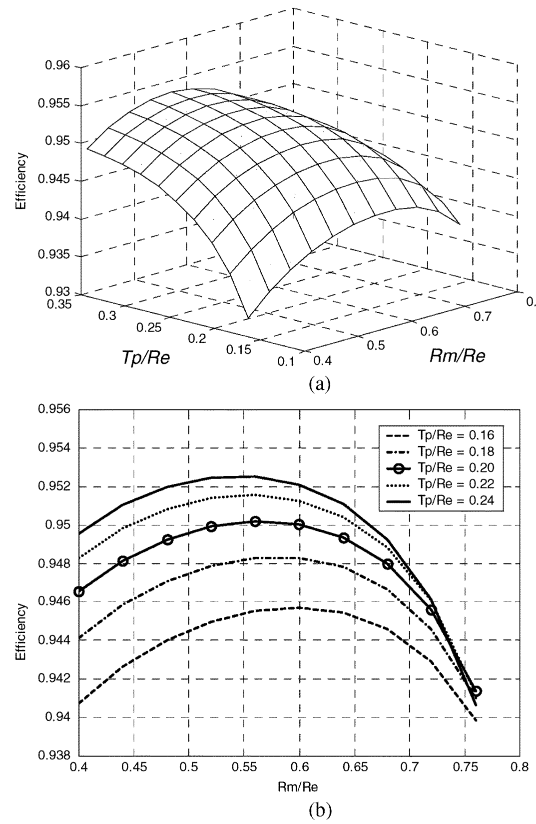


Fig. 18. Variation of efficiency with $R_m/R_e$ and $\tau_p/R_e$, for $\tau_{\rm mr}/\tau_p = 0.6$. (a) 3-D representation. (b) 2-D representation.

magnetic loading of the machine for a given thermal performance. Similarly, for a given value of $R_m/R_e$, an optimum $\tau_p/R_s$ ratio exists which results in the maximum force density. As the ratio of $\tau_p/R_e$ is reduced below the optimum value, the air-gap field which is produced by the permanent magnets decays more rapidly with radius and interpole flux leakage also increases. Hence, the force capability reduces. However, if the ratio of $\tau_p/R_e$ is too large, the flux per pole increases and this results in increased saturation of both the stator and armature cores if their radii are maintained constant, or requires thicker cores if their operating flux density is to be maintained constant. In both cases, the force density again reduces. The optimal dimensional ratios to achieve the maximum force density of 324.0 kN/m$^3$ are $R_m/R_e = 0.52$ and $\tau_p/R_e = 0.2$.

Fig. 17 shows the variation of the specific force (i.e., force per unit mass) as a function of the dimensional ratios $R_m/R_e$ and $\tau_p/R_e$. A similar trend is observed, in that for a given $\tau_p/R_e$ ratio there exists an optimal value of $R_m/R_e$ which yields the maximum specific force. However, this optimal ratio increases as $\tau_p/R_e$ decreases. This is due to the fact that, for a given outer radius $R_e$ and pole pitch $\tau_p$, the total weight of the machine reduces as the ratio $R_m/R_e$ is increased.

Figs. 18 and 19 respectively show the variation of the machine efficiency and power factor as functions of the two-dimensional ratios $R_m/R_e$ and $\tau_p/R_e$. As will be seen, optimal ratios of $R_m/R_e = 0.52$ and $\tau_p/R_e = 0.32$ exist which yield the maximum machine efficiency of 0.954. This trend is similar to that which was observed in Fig. 16, although the optima occur at

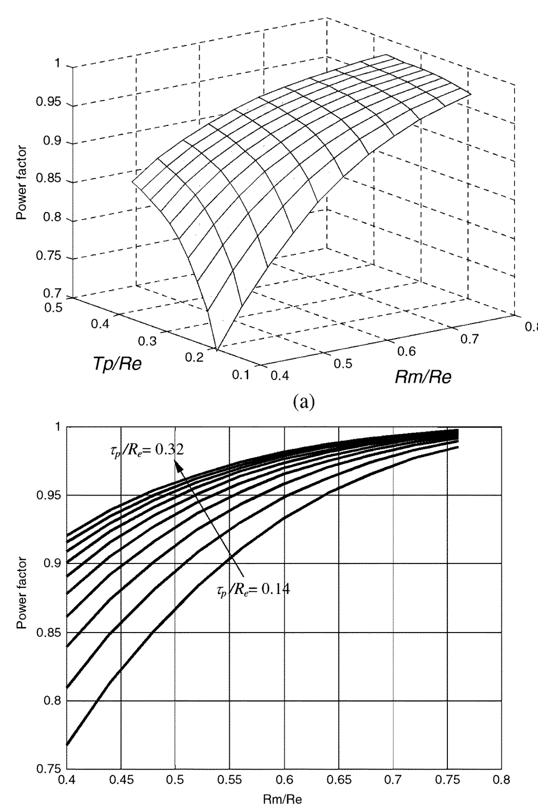


Fig. 19. Variation of specific force with $R_m/R_e$ and $\tau_p/R_e$, for $\tau_{\rm mr}/\tau_p = 0.6$. (a) 3-D representation. (b) 2-D representation.

slightly different dimensional ratios. It should be noted that the power factor increases as both ratios are increased. This is due

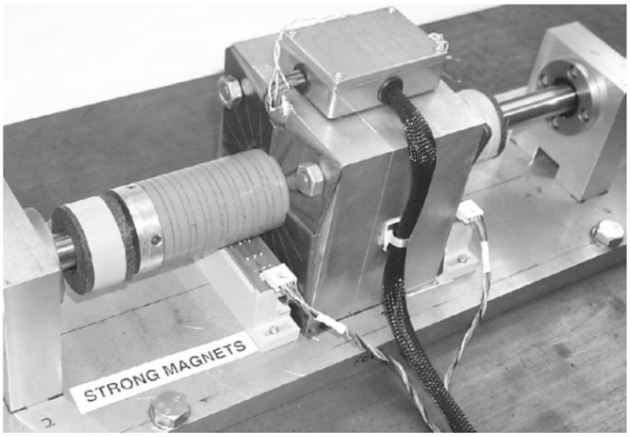


Fig. 20. Prototype three-phase tubular modular PM machine.

TABLE III
DESIGN SPECIFICATION OF PROTOTYPE MACHINE

| | |
|---|---|
| Thrust force (N) | 250 |
| Efficiency | >0.94 |
| Power factor | >0.92 |
| DC link voltage (V) | 320 |
| Rated current (rms A) | 4.35 |
| Ambient temperature ($^0$C) | 40 |
| Maximum temperature rise ($^0$C) | 100 |
| Surface convection coefficient (W/$^0$C /m$^2$) | 20 |
| Rated velocity (m/s) | 6 |

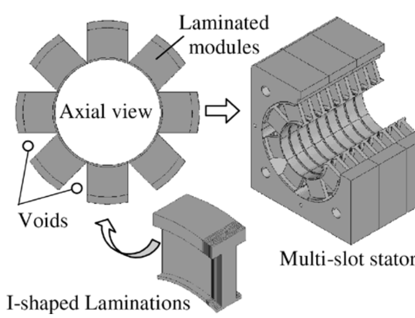


Fig. 21. Slotted stator core for prototype three-phase tubular modular PM machine.

to the fact that the slot-leakage inductance accounts for a large portion of the machine inductance, and it decreases as the slot depth is reduced with an increase in $R_m$ and as the slot width is increased with an increase in $\tau_p$.

## V. Prototype and Experimental Results

Fig. 20 show a prototype 10-pole, 9-slot, three-phase tubular modular PM machine, with a quasi-Halbach magnetization, whose specification is given in Table III. The stator core is fabricated from I-shaped silicon iron laminations, as illustrated in Fig. 21, with the coils being inserted into the slots as the core is assembled. The complete stator assembly is vacuum impregnated with stycast and is accommodated in a rectangular aluminum housing. The moving-magnet armature is supported at both ends by linear ball bearings. The leading design parameters of the machine are given in Table IV. As can be seen, the key dimensional ratios have been chosen to achieve the maximum force capability.

TABLE IV
LEADING DESIGN PARAMETERS OF PROTOTYPE MACHINE

| | |
|---|---|
| Outer stator radius $R_e$ (m) | 0.05 |
| Outer radius of magnets (m) | 0.0245 |
| Magnet thickness $h_m$ (m) | 0.005 |
| Pole-pitch $\tau_p$ (m) | 0.01 |
| $\tau_{mr}/\tau_p$ ratio | 0.6 |
| Air-gap length $G$ (m) | 0.001 |
| Number of pole-pairs $p$ | 5 |
| Number of slots $N_s$ | 9 |
| Number of turns per half coil $N_c$ | 30 |

TABLE V
MEASURED AND PREDICTED PHASE RESISTANCE AND SYNCHRONOUS INDUCTANCE

| | Measured | Predicted | |
|---|---|---|---|
| | | Analytical | FE |
| Phase resistance (at 25 C$^o$, $\Omega$) | 0.97 | 0.94 | - |
| Synchronous inductance (mH) | 4.52 | 4.70 | 4.81 |

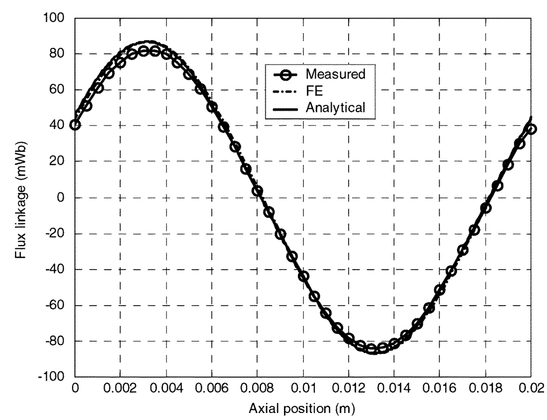


Fig. 22. Variation of measured and predicted flux-linkage with axial position.

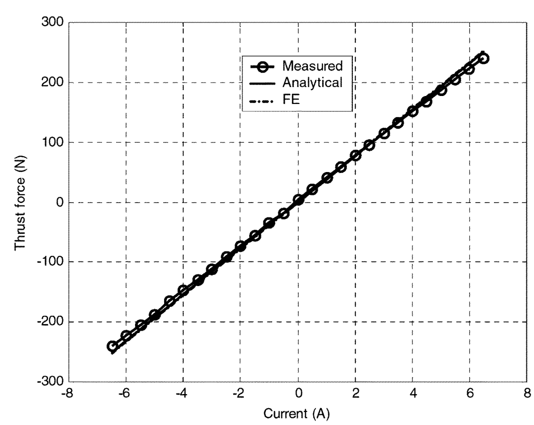


Fig. 23. Comparison of measured and predicted thrust force as a function of peak phase current.

Table V compares the measured and predicted phase resistance and synchronous inductance. The flux-linkage waveform of each phase has been measured using a flux meter and linear position encoder, the measured results being compared with analytical and FE predictions in Fig. 22. As can be seen, there is a very small asymmetry in the measured flux linkage, which is probably due to drift of the flux meter. In general, however, the measured flux-linkage waveform agrees very well with the predicted waveform, albeit its magnitude being $\sim 2\%$ lower.

The static thrust force capability of the machine was measured at a fixed armature displacement by using a force transducer and supplying each phase with an appropriate dc current. Since the machine design incorporates optimally profiled stator core-end surfaces so as to minimize the cogging force component associated with the finite axial length, the peak-to-peak cogging force of the machine is relatively small. Nevertheless, the cogging force and frictional force characteristic was measured separately, so that these parasitic forces could be subtracted from the measured thrust force at any given armature position. Fig. 23 compares the variation of the measured and predicted thrust force with peak phase current. As will be seen, measurements again agree well with predictions, and the machine exhibits a linear variation of thrust force with current, up to its rated value.

## VI. Conclusion

Alternative winding configurations for three-phase tubular modular PM machines, and the associated space MMF harmonic distributions, have been analyzed, and a general analytical framework for predicting the armature reaction field and the machine self- and mutual inductances has been established. The utility and accuracy of the analytical formulas for predicting the open-circuit EMF, thrust force, and armature reaction field for machines equipped with quasi-Halbach magnetized magnets have been verified by extensive finite-element analysis. It has been shown that the design of a machine can be optimized with respect to three key dimensional ratios, and an optimization methodology has been described. It has been shown that an optimal ratio of $\tau_{\mathrm{mr}}/\tau_p$, i.e., the ratio of the axial length of the radially magnetized magnets to the pole pitch, exists which yields maximum force capability. It has also been shown that this ratio has a significant influence on the fifth and seventh EMF harmonics, and hence on the peak-to-peak ripple in the thrust force. However, the force ripple is a minimum when $\tau_{\mathrm{mr}}/\tau_p = 0.7$, irrespective of the other design parameters. The validity and the effectiveness of the developed analysis and design optimization technique have been demonstrated on a 10-pole, 9-slot, three-phase tubular modular PM machine.

## References


[1] J. Wang and D. Howe, "Design optimization of radially magnetized, iron-cored, tubular permanent magnet machines and drive systems," *IEEE Trans. Magn.*, vol. 40, no. 5, pp. 3262–3277, Sep. 2004.

[2] Y. Amara, J. Wang, and D. Howe, "Stator iron loss of tubular permanent magnet machine," *IEEE Trans. Ind. Appl.*, vol. 41, no. 4, pp. 989–995, Jul.–Aug. 2005.

[3] J. Wang, G. W. Jewell, and D. Howe, "A general framework for the analysis and design of tubular linear permanent magnet machines," *IEEE Trans. Magn.*, vol. 35, no. 3, pp. 1986–2000, May 1999.

[4] J. Wang, Y. Amara, and D. Howe, "Armature reaction field and inductances of tubular modular permanent magnet machines," *J. Appl. Phys.*, to be published.

[5] Z. Q. Zhu and D. Howe, "Instantaneous magnetic field distribution in brushless permanent magnet dc motors—Part II: Armature reaction field," *IEEE Trans. Magn.*, vol. 29, no. 1, pp. 136–142, Jan. 1993.

[6] J. Wang, M. Innoue, Y. Amara, and D. Howe, "Cogging force reduction techniques for tubular permanent magnet machines," *Proc. Inst. Elect. Eng.—Elect. Power Appl.*, vol. 152, no. 3, pp. 731–738, May 2005.


Manuscript received March 23, 2005; revised June 10, 2005.

**Jiabin Wang** (SM'03) was born in Jiangsu Province, China, in 1958. He received the B.Eng. and M.Eng. degrees in electrical and electronic engineering from Jiangsu University of Science and Technology, Zhengjiang, China, in 1982 and 1986, respectively, and the Ph.D. degree in electrical and electronic engineering from the University of East London, London, U.K., in 1996.

Currently, he is a Senior Lecturer at the University of Sheffield, Sheffield, U.K. From 1986 to 1991, he was with the Department of Electrical Engineering at Jiangsu University of Science and Technology, where he was appointed a Lecturer in 1987 and an Associated Professor in 1990. He was a Postdoctoral Research Associate at the University of Sheffield, Sheffield, U.K., from 1996 to 1997, and a Senior Lecturer at the University of East London from 1998 to 2001. His research interests range from motion control to electromagnetic devices and drive systems.

**David Howe** received the B.Tech. and M.Sc. degrees in electrical power engineering from the University of Bradford, Bradford, U.K., in 1966 and 1967, respectively, and the Ph.D. degree in electrical power engineering from the University of Southampton, Southampton, U.K.

Currently, he is a Professor of Electrical Engineering at the University of Sheffield, Sheffield, U.K., where he heads the Electrical Machines and Drives Research Group. He has held academic posts at Brunel University, London, U.K., and Southampton University, and spent a period in industry with NEI Parsons Ltd., Newcastle-Upon-Tyne, U.K., working on electromagnetic problems related to turbogenerators. His research activities span all facets of controlled electrical drive systems with particular emphasis on permanent-magnet-excited machines.

Dr. Howe is a Fellow of the Institution of Electrical Engineers, U.K., and Fellow of the Royal Academy of Engineering, U.K.